

High-power ～ 4.1 μm quantum cascade lasers grown by metal-organic chemical vapor deposition

Chao Wang(王超), Chenhao Qian(钱晨灏), Yang Cheng(程洋), Junpu Wang(王俊普), Xiaoyue Luo(罗晓玥), Yuhang Zhang(章宇航), Wu Zhao(赵武), Fangyuan Sun(孙方圆), and Jun Wang(王俊)
Citation: Chin. Phys. B, 2025, 34 (**7**): 074204. DOI: 10.1088/1674-1056/adcdea
http://cpb.iphy.ac.cn; http://iopscience.iop.org/cpb

What follows is a list of articles you may be interested in

High peak power mini-array quantum cascade lasers operating in pulsed mode

Yuhang Zhang(章宇航), Yupei Wang(王渝沛), Xiaoyue Luo(罗晓玥), Chenhao Qian(钱晨灏), Yang Cheng(程洋), Wu Zhao(赵武), Fangyuan Sun(孙方圆), Jun Wang(王俊), and Zheng-Ming Sun(孙正明)
Chin. Phys. B, 2025, 34 (**1**): 014204. DOI: 10.1088/1674-1056/ad886b

Broadband third-order optical nonlinearities of layered franckeite towards mid-infrared regime

Zhi-Qiang Xu(徐志强), Tian-Tian Zhou(周甜甜), Jie Li(李洁), Dong-Yang Liu(刘东阳), Yuan He(何源), Ning Li(李宁), Xiao Liu(刘潇), Li-Li Miao(缪丽丽), Chu-Jun Zhao(赵楚军), and Shuang-Chun Wen(文双春)
Chin. Phys. B, 2024, 33 (**10**): 104208. DOI: 10.1088/1674-1056/ad6ccb

Third-order nonlinear wavelength conversion in chalcogenide glass waveguides towards mid-infrared photonics

Fengbo Han(韩锋博), Jiaxin Gu(顾佳新), Lu Huang(黄璐), Hang Wang(王航), Yali Huang(黄雅莉), Xuecheng Zhou(周学成), Shaoliang Yu(虞绍良), Zhengqian Luo(罗正钱), Zhipeng Dong(董志鹏), and Qingyang Du(杜清扬)
Chin. Phys. B, 2024, 33 (**10**): 104207. DOI: 10.1088/1674-1056/ad6557

Surface phonon resonance: A new mechanism for enhancing photonic spin Hall effect and refractive index sensor

Jie Cheng(程杰), Chenglong Wang(汪承龙), Yiming Li(李一铭), Yalin Zhang(张亚林), Shengli Liu(刘胜利), and Peng Dong(董鹏)
Chin. Phys. B, 2024, 33 (**8**): 084201. DOI: 10.1088/1674-1056/ad4a3c

A 3-5 μm broadband YBCO high-temperature superconducting photonic crystal

Gang Liu(刘刚), Yuanhang Li(李远航), Baonan Jia(贾宝楠), Yongpan Gao(高永潘), Lihong Han(韩利红), Pengfei Lu(芦鹏飞), and Haizhi Song(宋海智)
Chin. Phys. B, 2023, 32 (**3**): 034213. DOI: 10.1088/1674-1056/acb760

High-power ~ 4.1 μm quantum cascade lasers grown by metal-organic chemical vapor deposition

Chao Wang(王超)[1,†], Chenhao Qian(钱晨灏)[1], Yang Cheng(程洋)[4,5], Junpu Wang(王俊普)[4], Xiaoyue Luo(罗晓玥)[2], Yuhang Zhang(章宇航)[3], Wu Zhao(赵武)[5], Fangyuan Sun(孙方圆)[2,5], and Jun Wang(王俊)[2,4,5,‡]

[1] *Faculty of Electronic Information Engineering, Huaiyin Institute of Technology, Huaian* 201800, *China*
[2] *College of Electronic Information, Sichuan University, Chengdu* 610041, *China*
[3] *Southeast University–Monash University Joint Graduate School (Suzhou), Southeast University, Suzhou* 215125, *China*
[4] *National University of Defense Technology, Changsha* 410073, *China*
[5] *Suzhou Everbright Photonics Co., Ltd., Suzhou* 215009, *China*

(Received 21 January 2025; revised manuscript received 11 April 2025; accepted manuscript online 17 April 2025)

The authors report the development of a $\lambda \sim 4.1$ μm quantum cascade laser grown by metal-organic chemical vapor deposition using strain-balanced InGaAs/InAlAs materials. A device with a 7.5 mm cavity length and 6.5 μm ridge width, bonded to an aluminum nitride heatsink, achieves maximum output powers of 3.4 W at 288 K in pulsed mode and 1.6 W at 288 K in continuous-wave (CW) operation, with corresponding maximum wall-plug efficiencies of 14.8% and 9.3%. A kink is observed in the power–current curve under CW operation, which is absent in pulsed operation. Near-field results show that in CW operation, the horizontal beam quality factor M^2 fluctuates with current, indicating mode instability and high-order lateral mode excitation, while in pulsed mode, the horizontal M^2 remains stable around 1.3 as the current increases from 1.4 A to 1.9 A.

Keywords: mid-infrared, quantum cascade laser, metal-organic chemical vapor deposition, beam quality

PACS: 42.55.Px, 42.60.Pk, 95.85.Hp

DOI: 10.1088/1674-1056/adcdea **CSTR:** 32038.14.CPB.adcdea

1. Introduction

In 1994, Faist *et al.*[1] reported the world's first quantum cascade laser (QCL), thereby significantly extending the wavelength range of semiconductor lasers. Initially, the primary growth technique for QCLs was molecular beam epitaxy (MBE), which facilitated precise control over growth thickness and interface quality through *in situ* monitoring.[2–11] However, MBE technology faces issues such as high costs and low growth efficiency.[12] Metal-organic chemical vapor deposition (MOCVD) is a gas-phase reaction under low-pressure conditions, and its growth switching exhibits a delay effect. Therefore, the heterojunction interfaces grown by MOCVD have poorer steepness compared to those grown by MBE. However, MOCVD equipment is easy to maintain, highly reproducible, efficient for growth, and suitable for large-scale production, making it more promising for commercialization. Roberts *et al.*[13] first applied MOCVD to QCL material preparation. Since then, numerous research groups have focused on MOCVD-grown QCLs,[14–21] with Watt-level QCL at lasing wavelengths near 5 μm being reported. Notably, Botez *et al.*[22] achieved a maximum output power of 2.6 W for a $\lambda \sim 5$ μm QCL under continuous room-temperature conditions in 2018. In 2023, Liu *et al.*[23] reported a $\lambda \sim 4.6$ μm QCL with a maximum output power of 3 W under similar conditions, marking one of the most outstanding results to date for MOCVD-grown QCLs. In contrast, reports concerning $\lambda \sim 4$ μm QCLs grown by MOCVD are relatively scarce. In 2012, Xie *et al.*[24] presented a 4 μm emitting QCL grown by MOCVD, which exhibited a continuous-wave (CW) output power of approximately 0.6 W and a wall-plug efficiency (WPE) of 5.5% at 288 K. Given that the 4 μm band is situated for the low-loss atmospheric window and possesses a broad range of applications, conducting research on $\lambda \sim 4$ μm Watt-level QCLs grown by MOCVD holds considerable significance.

We report a 4 μm emitting mid-infrared QCL grown by MOCVD, with a cavity length of 7.5 mm and a ridge width of 6.5 μm. At a temperature of 288 K, it achieves a power of 3.4 W in pulsed mode, with a maximum WPE of 14.8%. In CW operation, the output power reaches 1.6 W, with a WPE of 9.3%. Moreover, the research findings indicate that the kink observed in the power–current (*P*–*I*) curve is predominantly attributed to optical mode instability. This instability is primarily caused by thermal effects and the excitation of high-order lateral modes.

2. Device fabrication

The epitaxial structure is shown in Fig. 1. The QCLs investigated in this study are grown by MOCVD in a reactor

†Corresponding author. E-mail: chaowang@hyit.edu.cn
‡Corresponding author. E-mail: wjdz@scu.edu.cn

© 2025 Chinese Physical Society and IOP Publishing Ltd. All rights, including for text and data mining, AI training, and similar technologies, are reserved.

equipped with a close-coupled showerhead injector. Starting from the substrate, the following epitaxial layers are grown sequentially: a 0.5 μm InP buffer layer, a 3 μm low-doped InP cladding layer, a 0.1 μm InGaAs waveguide layer, a 30-period strain-balanced InGaAs/InAlAs active region, a 0.1 μm InGaAs waveguide layer, a 3.5 μm low-doped InP cladding layer, and a 1 μm heavily doped InP cap layer. The reported non-resonant extraction active region[7,9] has been modified with the aim of achieving a lasing wavelength of 4.0 μm.

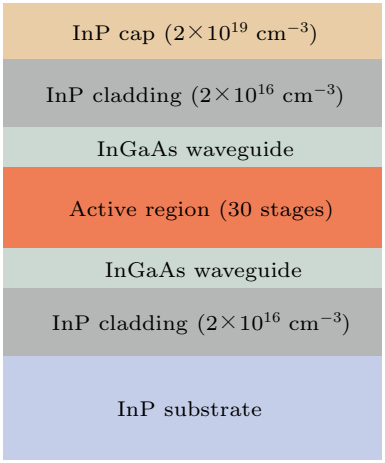


Fig. 1. Schematic diagram of the epitaxial structure of the QCL.

Following the growth process, a high-resolution double-crystal x-ray diffractometer (XRD) was employed to assess the quality of the epitaxial layers, and the x-ray diffraction spectrum is shown in Fig. 2(a). Upon examining the magnified image, the sample displays distinct and sharp peaks. Notably, the full width at half maximum (FWHM) of the diffraction satellite peak is remarkably low, measuring only 21 arcseconds (Fig. 2(b)). This observation signifies that the active region material possesses a sharply defined heterojunction interface. Furthermore, it indicates minimal interface roughness and attests to the superior growth quality of the sample.

A buried hetero-structure configuration is subsequently fabricated from the epitaxial wafer, characterized by a ridge width of 6.5 μm. Initially, the epitaxial wafer is subjected to wet etching through the active region to achieve a double-channel geometry, employing a 300 nm SiO_2 mask as the etching template. Thereafter, the channels are planarized through selective-area regrowth of Fe-doped semi-insulating InP by using MOCVD. A 300 nm Si_3N_4 layer is subsequently deposited as an insulating layer via plasma-enhanced chemical vapor deposition. Following this, a Ti/Pt/Au layer is sputtered onto the surface and annealed to form an ohmic contact. In order to enhance heat dissipation, a 4 μm thick gold layer is electroplated onto the structure. Subsequent to substrate thinning and polishing, a Ge/Au/Ni/Au layer is deposited to serve as the back electrode. Scanning electron microscope (SEM) measurements reveal a ridge width of 6.5 μm, as depicted in Fig. 3.

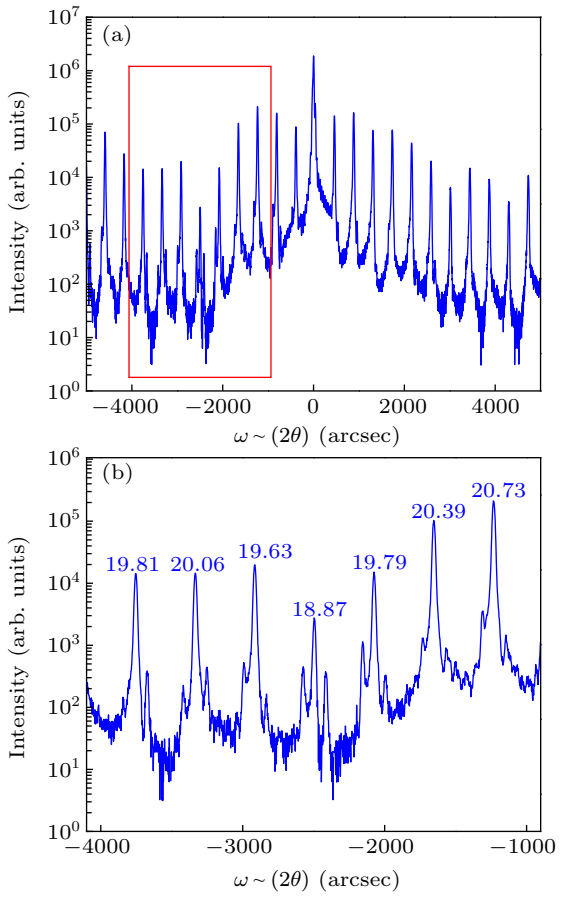


Fig. 2. (a) X-ray double-crystal diffraction of $\omega \sim (2\theta)$ test result. (b) Enlarged image of the x-ray double-crystal diffraction test results (red box).

The wafer is subsequently processed into individual devices, each featuring distinct cavity lengths, namely, 3 mm, 4 mm, 5 mm, and 7.5 mm. Chips with shorter cavity lengths (3 mm, 4 mm, and 5 mm) are left uncoated and are intended for the characterization of the wafer's intrinsic physical parameters, such as waveguide loss and internal quantum efficiency. In contrast, chips with a 7.5 mm cavity length are coated; specifically, the front facet is coated with an anti-reflection film, while the back facet is coated with a high-reflection film. For packaging purposes, the chips are soldered epi-down onto aluminum nitride heatsinks, a configuration designed to enhance the efficiency of heat removal.

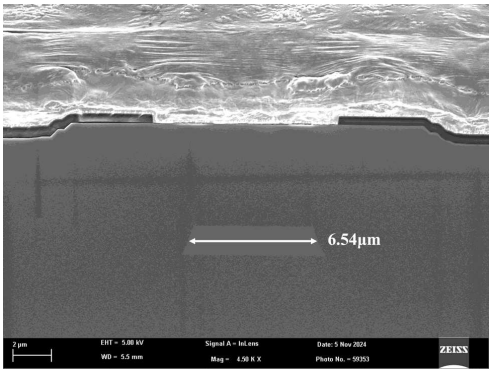


Fig. 3. SEM of the ridge width of the sample.

3. Device performance and result analysis

After packaging, the device is characterized for performance. Power collection is performed using a Gentec power meter, voltage data is collected using a Keysight voltage oscilloscope, spectral testing is conducted with a Thermo Scientific Nicolet iS50R Fourier transform infrared spectrometer with a resolution set to 0.125 cm^{-1}, and near-field beam images are captured using a DataRay WinCamD-IR-BB infrared beam profiler. Chips with shorter cavity lengths (3 mm, 4 mm, and 5 mm) are obtained through cleaving. The two facets are uncoated, and only the naturally cleaved atomic surfaces are present. At 288 K, the internal loss α_i and internal quantum efficiency η_i of the samples are tested. A linear fitting is performed based on the inverse relationship between cavity length and external quantum efficiency, with the fitting formula given by

$$\frac{1}{\eta_{ext}} = \frac{2\alpha_i L}{\eta_i \ln(1/(R_1R_2))} + \frac{1}{\eta_i}, \tag{1}$$

where R_1 and R_2 are the reflectivities of the two facets, and η_{ext} is the external quantum efficiency.

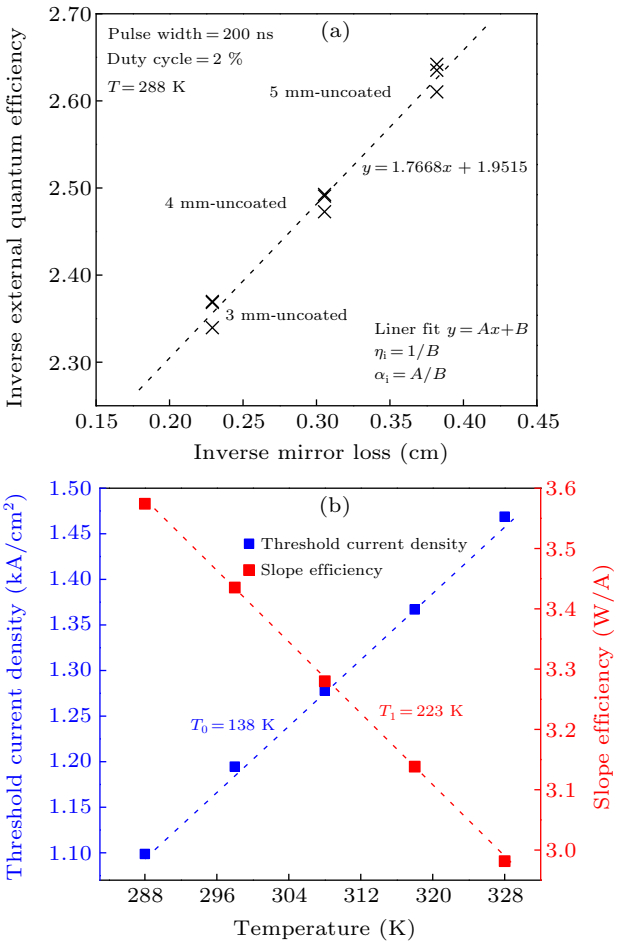


Fig. 4. (a) The relationship between external quantum efficiency and mirror loss. (b) Threshold current density and slope efficiency at different temperatures in pulse conditions at 200 ns, 2% duty cycle.

The experimental conditions include a pulse width of 200 ns and 2% duty cycle. The relationship between internal quantum efficiency and internal loss, as shown in Fig. 4(a), is derived from the experimental results of multiple devices, and the external quantum efficiency is linearly related to mirror loss. The internal quantum efficiency of the 6.5 μm ridge width device is 51.2%, and the internal loss is 0.9 cm^{-1}. Low internal loss can reduce the absorption and scattering of photons within the cavity, thereby increasing the output power and overall efficiency of the device. Figure 4(b) shows the relationship between the threshold current density and slope efficiency at different temperatures under a pulse width of 200 ns and a duty cycle of 2%. The experimental relationship is

$$J_{th} = J_0 \exp(T/T_0), \tag{2}$$

$$\eta_s = \eta_0 \exp(-T/T_1), \tag{3}$$

where T is the heat sink temperature. The characteristic temperatures of threshold current density (T_0) and slope efficiency (T_1) in pulsed mode are calculated through exponential fitting, yielding values of 133 K and 208 K, respectively. Smaller T_0 indicates that the laser is more sensitive to temperature changes, with a greater variation in threshold current with temperature.[25]

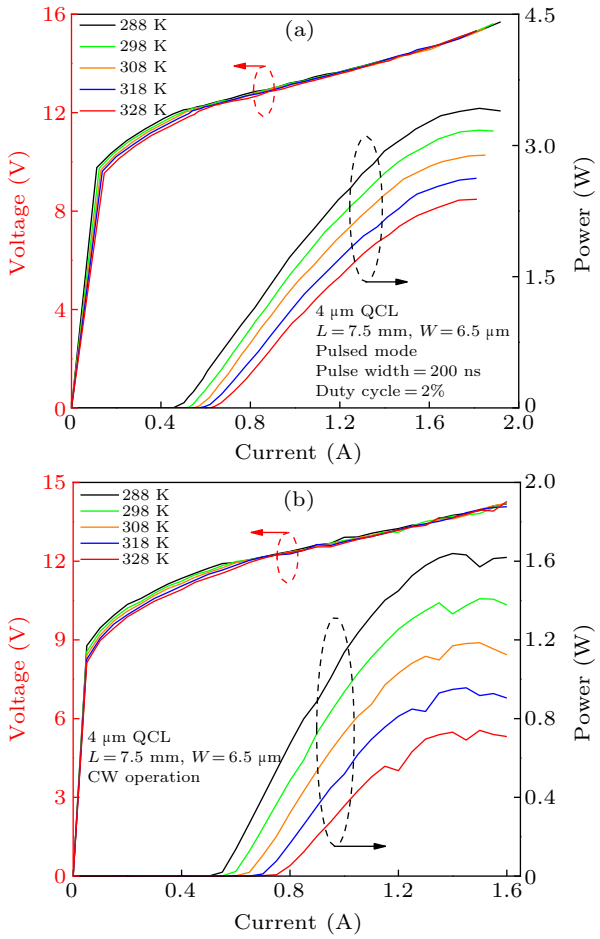


Fig. 5. The *P–I–V* experimental results at different temperatures, with the chip mounted epilayer-down on an AlN heatsink. (a) Pulsed mode (200 ns, 100 kHz); (b) CW operation.

The device with a 7.5 mm cavity length is subjected to *P–I–V* testing from 288 K to 328 K. Figure 5(a) displays the

pulsed mode results, using 200 ns pulse width at a 2% duty cycle. At 288 K, the device exhibits a peak power of 3.4 W, a threshold current of 0.5 A, a slope efficiency of 3.6 W/A, and a maximum WPE of 14.8%. With increasing temperature, the threshold current rose, and both slope and WPE declined. At 328 K, the threshold current is 0.64 A, the slope efficiency is 3.0 W/A, the maximum power is 2.4 W, and the maximum WPE is 9.9%.

The *P–I–V* characteristics for CW operation are shown in Fig. 5(b). At 288 K, the chip achieved a maximum power of 1.6 W, with a threshold current of 0.57 A, a maximum slope efficiency of 2.6 W/A, and a maximum WPE of 9.3%. As the temperature increased to 328 K, the threshold current increased to 0.78 A, the slope efficiency decreased to 1.4 W/A, and the WPE fell to 4%. Compared to pulsed mode, the chip in CW operation shows a higher threshold current and lower slope efficiency. This is mainly due to the difficulty in dissipating heat generated in CW operation, which raises the active region temperature, increasing carrier leakage and limiting optical output power. From 288 K to 328 K, a noticeable kink appears in the *P–I* curve under CW operation as the driver current reaches 1.45 A, as shown in Fig. 5(b), the kink current decreases with increasing temperature. In contrast, the pulsed mode *P–I* curve in Fig. 5(a) shows no kink.

To further examine the cause of the kink appearing in the CW *P–I* curve, spectral and far-field distribution measurements are conducted at different currents to observe spectral changes and beam divergence angles under high current conditions. Figure 6 shows the CW spectrum of the device at different currents at 288 K. The device emits in multiple longitudinal modes, with a broad spectral range and a centroid wavelength of 4.08 μm. At 1.45 A (where the kink appears in the *P–I* curve), the spectrum undergoes significant changes, broadening and splitting into two spectral sub-groups, while the centroid wavelength blue-shifts to 4.04 μm. The sub-groups observed in the spectrum at 1.45 A may result from the coexistence of multiple lateral modes that are not yet phase-synchronized.[26] Each lateral mode forms its own longitudinal comb with slightly different spacing due to variations in refractive index. The partial overlap of these unsynchronized combs produces clustered spectral features, seen as mode sub-groups.

Figure 7 shows the far-field distribution of the device with a 7.5 mm cavity length at different currents under CW operation. It is observed that as the current increases, the FWHM of the slow axis increases from 24.5° to 27.8°, and the FWHM of the fast axis increases from 31.7° to 39°. The increase in the divergence angle is attributed to the enhanced thermal effects caused by the increase in current, with the influence of higher-order lateral modes continuously increasing.[27,28] However, it seems that the proportion of higher-order lateral modes is relatively small, there is no significant change in the far-field distribution.

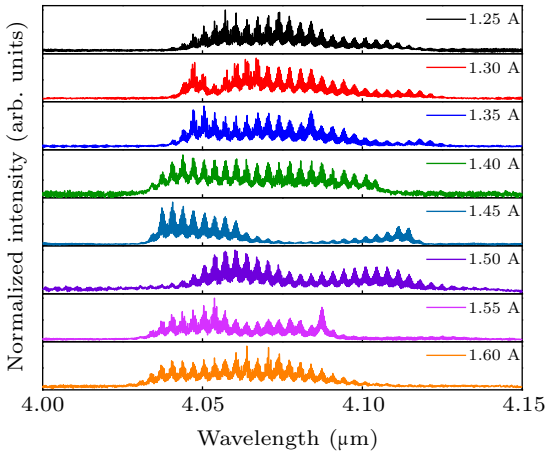


Fig. 6. Spectrum of the device with a 7.5 mm cavity length at different currents under CW operation.

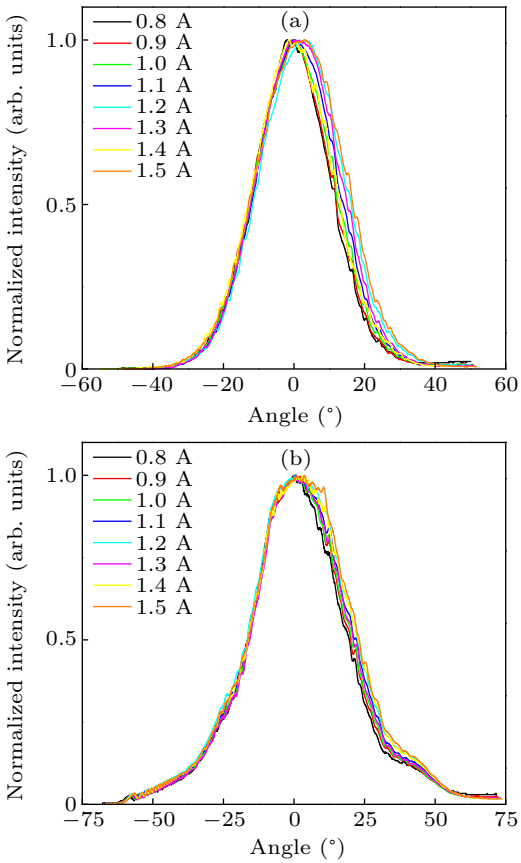


Fig. 7. Far-field of device with a 7.5 mm cavity length at different currents under CW operation; (a) slow axis; (b) fast axis.

The presence of high-order lateral modes typically degrades laser beam quality. To assess this, a collimating lens is placed before the device to collimate the beam, and the near-field distribution and beam quality factor M^2 are measured and calculated at different currents and 288 K. The calculation formula is as follows:

$$M^2 = \frac{\pi\omega\theta}{\lambda}, \tag{4}$$

where θ and ω are the far-field divergence angle and the minimum beam waist radius of the beam, respectively.

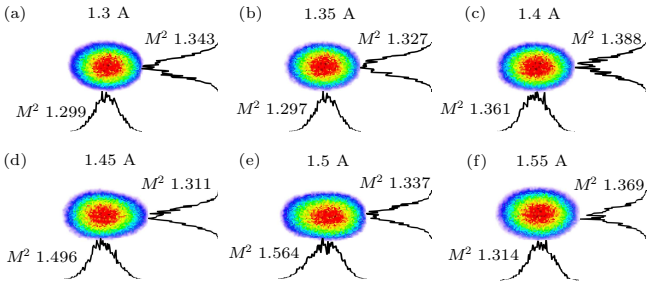


Fig. 8. Near-field of the device and M^2 at different currents in CW operation. The test currents for (a) to (f) are from 1.3 A to 1.55 A, with a step of 50 mA.

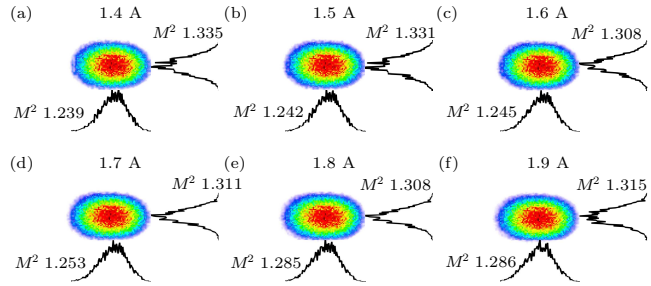


Fig. 9. Near-field of the device and M^2 at different currents in pulse mode (200 ns, 100 kHz). The test currents for (a) to (f) are from 1.4 A to 1.9 A, with a step of 100 mA.

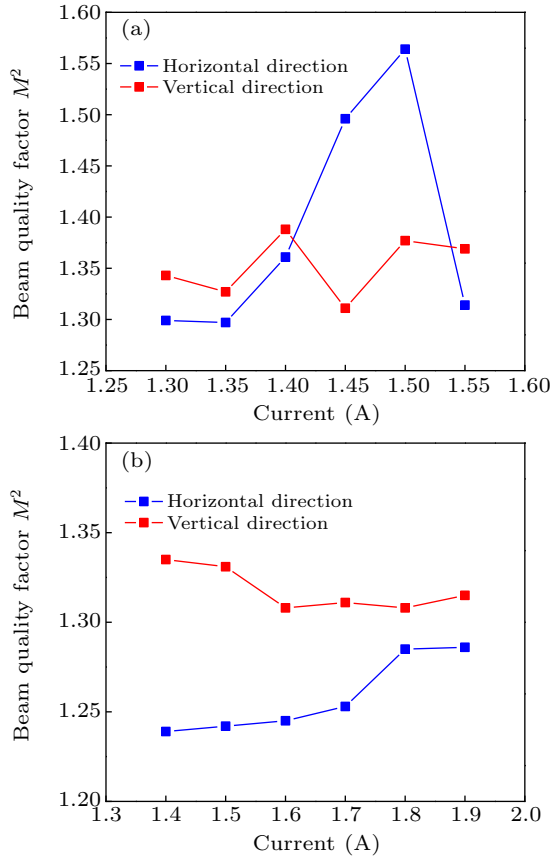


Fig. 10. Beam quality factor M^2 of device with a 7.5 mm cavity length at different currents; (a) CW operation; (b) pulsed mode.

The near-field distribution of the 7.5 mm cavity length device in CW operation is depicted in Fig. 8. As the current increases from 1.3 A to 1.55 A, the M^2 in the vertical direction (epitaxial growth direction) remains constant at approximately 1.35, and the horizontal M^2 stays around 1.3, until at 1.45 A where it rises to 1.5 (Fig. 10(a)), indicating the emergence of high-order lateral modes, the decrease in horizontal M^2 observed as the current increases from 1.5 A to 1.55 A can be attributed to the onset of nonlinear phase locking among lateral modes. As these modes begin to synchronize in phase and frequency, they constructively interfere to produce a more coherent and collimated output beam. This process, known as beam steering, leads to a noticeable enhancement in the beam quality and a reduction in divergence.[26] In contrast, as shown in Fig. 9, in pulsed mode, the M^2 value remains stable at around 1.3 across the entire current range (Fig. 10(b)), indicating the absence of high-order lateral modes. It is concluded that the kink observed in the CW *P–I* curve can be attributed to mode instability and the excitation of high-order lateral modes, which are predominantly induced by thermal effects.

4. Conclusion and perspectives

In summary, this paper presents a 4 μm emitting mid-infrared QCL fabricated via MOCVD. The device utilizes strain-balanced InGaAs/InAlAs materials, with a 7.5 mm cavity length and a 6.5 μm ridge width. It operates at a lasing wavelength of 4.08 μm and supports CW operation at room temperature. At 288 K, the device achieves 3.4 W output power in pulsed mode with a WPE of 14.8%, and 1.6 W in CW operation with a WPE of 9.3%. At 328 K, the CW output power remains above 0.7 W. The kink in the CW *P–I* curve is attributed to optical mode instability and high-order lateral mode excitation due to thermal effects. Spectral and far-field measurements indicate that higher-order lateral modes cause spectral broadening, peak splitting, and increased divergence angles, degrading beam quality. Near-field tests further demonstrate that in CW operation, the horizontal M^2 stays around 1.3, until at 1.45 A where it rises to 1.5, indicating the emergence of high-order lateral modes. This research is of significant importance for the achievement of Watt-level $\lambda \sim 4$ μm QCL grown by MOCVD.

Acknowledgment

The authors thank Zhixiang Wei and Diyi Han for their help in device processing.

References

[1] Faist J, Capasso F, Sivco D L, Sirtori C, Hutchinson A L and Cho A Y 1994 *Science* **264** 553
[2] Faist J, Capasso F, Sirtori C, Sivco D L, Baillargeon J N, Hutchinson A L, Chu S N G and Cho A Y 1996 *Appl. Phys. Lett.* **68** 3680
[3] Faist J, Capasso F, Sivco D L, Hutchinson A L, Chu S N G and Cho A Y 1998 *Appl. Phys. Lett.* **72** 680
[4] Beck M, Hofstetter D, Aellen T, Faist J, Oesterle U, Ilegems M, Gini E and Melchior H 2002 *Science* **295** 301
[5] Evans A, Darvish S R, Slivken S, Nguyen J, Bai Y and Razeghi M 2007 *Appl. Phys. Lett.* **91** 071101

[6] Bai Y, Darvish S R, Slivken S, Zhang W, Evans A, Nguyen J and Razeghi M 2008 *Appl. Phys. Lett.* **92** 101105

[7] Lyakh A, Maulini R, Tsekoun A, Go R, Pflügl C, Diehl L, Wang Q J, Capasso F and Patel C K N 2009 *Appl. Phys. Lett.* **95** 141113

[8] Yu J S, Darvish S R, Evans A, Nguyen J, Silvken S and Razeghi M 2006 *Appl. Phys. Lett.* **88** 041111

[9] Lyakh A, Maulini R, Tsekoun A, Go R, Porten S V, Pflügl C, Diehl L, Capasso F and Patel C K N 2010 *Proc. Natl. Acad. Sci. USA* **107** 18799

[10] Lyakh A, Maulini R, Tsekoun A G, Go R and Patel C K N 2011 *Novel In-Plane Semiconductor Lasers X* **7953** 347

[11] Wang F, Slivken S, Wu D H, Lu Q Y and Razeghi M 2020 *Aip. Adv* **10** 055120

[12] Patel C K N, Troccoli M and Barron-Jimenez R 2019 *Technologies for Optical Countermeasures XVI* **11161** 1116102

[13] Roberts J S, Green R P, Wilson L R, Zibik E A, Revin D G, Cockburn J W and Airey R J 2003 *Appl. Phys. Lett.* **82** 4221

[14] Lyakh A, Pflügl C, Diehl L, Wang Q J, Capasso F, Wang X J, Fan J Y, Tanbun-Ek T, Maulini R, Tsekoun A, Go R and Patel C K N 2008 *Appl. Phys. Lett.* **92** 111110

[15] Troccoli M, Lyakh A, Fan J Y, Wang X J, Maulini R, Tsekoun A, Go R and Patel C K N 2013 *Opt. Mater. Express* **3** 1546

[16] Xie F, Caneau C, Leblanc H P, Caffey D P, Hughes L C, Day T and Zah C 2013 *IEEE. J. Sel. Top. Quantum* **19** 1200407

[17] Xie F, Caneau C G, LeBlanc H P, Ho M, Wang J, Chaparala S, Hughes L C and Zah C 2014 *Appl. Phys. Lett.* **104** 071109

[18] Schwarz B, Wang C A, Missaggia L, Mansuripur T S, Chevalier P, Connors M K, McNulty D, Cederberg J, Strasser G and Capasso F 2017 *ACS Photonics* **4** 1225

[19] Wang C A, Schwarz B, Siriani D F, Missaggia L J, Connors M K, Mansuripur T S, Calawa D R, McNulty D, Nickerson M, Donnelly J P, Creedon K and Capasso F 2017 *IEEE. J. Sel. Top. Quantum* **23** 1

[20] Fei T, Zhai S Q, Zhang J C, Zhuo N, Liu J Q, Wang L J, Liu S M, Jia Z W, Li K, Sun Y Q, Guo K, Liu F Q and Wang Z G 2021 *J. Semicond.* **42** 112301

[21] Sun Y Q, Yin R, Zhang J C, Liu J Q, Fei T, Li K, Guo K, Jia Z W, Liu S M, Lu Q Y, Zhuo N, Wang L J, Liu F Q and Zhai S Q 2022 *Opt. Express* **30** 37272

[22] Botez D, Kirch J D, Boyle C, Oresick K M, Sigler C, Kim H, Knipfer B B, Ryu J H, Lindberg D, Earles T, Mawst L J and Flores Y V 2018 *Opt. Mater. Express* **8** 1378

[23] Fei T, Zhai S Q, Zhang J C, Lu Q Y, Zhuo N, Liu J Q, Wang L J, Liu S M, Jia Z W, Li K, Sun Y Q, Guo K and Liu F Q 2023 *Photonics* **10** 47

[24] Xie F, Caneau C, LeBlanc H P, Visovsky N J, Chaparala S C, Deichmann O D, Hughes L C, Zah C, Caffey D P and Day T 2011 *IEEE. J. Sel. Top. Quantum* **17** 1445

[25] Lyakh A, Suttinger M, Go R, Figueiredo P and Todi A 2016 *Appl. Phys. Lett.* **109** 121109

[26] Wójcik A K, Yu N, Capasso F and Belyanin A 2011 *J. Mod. Opt.* **58** 727

[27] Bewley W W, Lindle J R, Kim C S, Vurgaftman I, Meyer J R, Evans A J, Yu J S, Slivken S and Razeghi M 2005 *IEEE J. Quantum Electron.* **41** 833

[28] Bai Y, Bandyopadhyay N, Tsao S, Selcuk E, Slivken S and Razeghi M 2010 *Appl. Phys. Lett.* **97** 25